Self-poled heteroepitaxial $Bi_{(1-x)}Dy_xFeO_3$ films with promising pyroelectric properties

*Quentin Micard, Giacomo Clementi, Ausrine Bartasyte, Paul Muralt, Guglielmo G. Condorelli, and Graziella Malandrino**

Quentin Micard,[1] Giacomo Clementi,[2] Ausrine Bartasyte,[2] Paul Muralt,[3] Guglielmo G. Condorelli,[1] and Graziella Malandrino [1,*]
[1] Dipartimento di Scienze Chimiche, Università di Catania, and INSTM UdR Catania, Viale A. Doria 6, I-95125 Catania, Italy. E-mail: gmalandrino@unict.it.
[2] FEMTO-ST Institute, University of Bourgogne Franche-Comté CNRS UMR 6174, 26 Rue de l'Epitaphe, F-25030 Besançon, France.
[3] Materials Institute, EPFL, Station 12, CH-1015, Lausanne, Switzerland.
E-mail: gmalandrino@unict.it

Keywords: $BiFeO_3$, thin films, hetero-epitaxial, ferroelectrics, pyroelectrics

Pyroelectric materials are very promising for thermal energy harvesting applications. To date, lead-based systems are the foremost studied materials in this field. A facile and simple metal organic chemical vapor deposition (MOCVD) route is applied for the fabrication of lead-free, high quality, epitaxial $Bi_{(1-x)}Dy_xFeO_3$ (x= 0, 0.06, 0.08, 0.11) thin films deposited on conductive $SrTiO_3$:Nb (100) single crystal substrates. The films are studied by structural, morphological, compositional and functional characterization. The correlation between the Dy-doping amount and the dielectric properties is thoroughly investigated. Unipolar PE loops and permittivity measurements show the important impact of Dy on ferroelectric, dielectric and pyroelectric properties. Dy doping increases considerably the dielectric response, but much more the pyroelectric coefficient, up to a concentration of 8% Dy. The films are self-poled, which is an ideal situation for pyroelectric applications. The best figure of merit for pyroelectric energy harvesting, F_E, is 82 J/(m^3K^2), showing a factor increase of 2.6 as compared to the undoped film of our sample series. It constitutes a factor 4.5 improvement as compared to previous results obtained on $BiFeO_3$ based thin films.

1. Introduction

Multiferroics are multifunctional oxides with fundamental physical properties that are very promising for potential applications in several fields: signal transduction, energy harvesting, sensors, memories and spintronics.[1] $BiFeO_3$ (BFO) and its related systems with their high ferroelectric and magnetic transition temperatures (T_C = 1103 K and T_N = 643 K) are of special interest,[2] as they maintain their ferroelectric, piezoelectric and pyroelectric properties even in an extreme temperature environment.

The development of BFO based energy harvesters has been mostly investigated for exploiting their photoelectric and piezoelectric properties.[3,4] Power generation employing the pyroelectric effect has been more rarely studied, and, in particular, previous works based on BFO thin films are limited to pure BFO, La-doped BFO or BFO/$Pb(Zr_xTi_{1-x})O_3$ bi-layers.[5] Pyroelectricity originates from a change of an internal polarization of the material, particularly of the spontaneous ferroelectric polarization, upon a temperature change.[6] This means that charges are generated together with a voltage depending on the capacitance of the pyroelectric capacitor. Pyroelectricity is thus of special interest for thermal energy harvesting, meaning the transformation of temperature fluctuations into electricity. These fluctuations occur in systems with time varying heat flows. In contrast to the thermoelectric effect, pyroelectricity does not need a thermal gradient, and thus a spatial temperature difference.[7,8] As leading materials for energy harvesting, $Pb(Zr_xTi_{1-x})O_3$ (PZT) and (1-x)$[Pb(Mg_{1/3}Nb_{2/3})O_3]$-x$[PbTiO_3]$ (PMN-PT) have been widely incorporated and combined with lead-free materials to tune their piezoelectric and pyroelectric properties,[9-13] but today the use of lead based materials raises environmental issues, which are always at the center of our attention. The answer is the development and integration of lead-free perovskite-like materials, such as $BiFeO_3$, $LiNbO_3$ [14-16] or $(K,Na)NbO_3$,[17] in energy harvesters.[18-20] The possibility of combining at least two of the previous properties in a single device, a hybrid energy harvester, makes BFO one of the most promising materials for the next generation of energy harvesters and, recently, some BFO-based energy harvesting devices have already been studied.[21-24] In general, pyroelectric properties of ceramics and single crystals have been intensively studied compared to thin films. Films present several advantages: with their smaller heat capacity, they are subjected to a larger temperature change upon a given heat input and are suitable for integration into microsystems.[25] Fine-tuned depositions can give high-quality materials and some deposition techniques offer good process scalability.[7,26] Among the above mentioned lead-free materials, BFO presents an intrinsic polarization of 60

$\mu C/cm^2$ and 100 $\mu C/cm^2$ along the $[001]_{pc}$ and $[111]_{pc}$ directions, respectively,[1,27] (pc stands for the pseudocubic unit cell), which makes it a perfect candidate to investigate its pyroelectric response.

Moreover, pyroelectricity is strongly influenced by material preparation conditions and a fine tuning of BFO thin film properties can be achieved in many ways. Numerous approaches have been reported: strained films,[28-29] modified synthesis parameters,[30,31] synthesis of BFO nanocomposites,[32-33] but, by far, the easiest and most used approach is the ionic substitution, which is achieved by doping BFO films with transition metals and/or rare-earth elements.[34-36] Doing so, BFO structure and properties can be widely modified, adapting and designing the material to different situations/use/working conditions and recent works have been focused on BFO A-site doping. BFO systems have been deposited on various substrates using pulsed laser deposition (PLD),[37-38] metal organic chemical vapor deposition (MOCVD),[39-43] sputtering,[44] sol-gel[45,46] and chemical solution deposition.[38,47]

In this study, we report on the promising pyroelectric properties of pure BFO and Dy-doped BFO (BDFO) films deposited, through a simple, easily scalable MOCVD approach, on Nb doped $SrTiO_3$ (STO:Nb) (001) single crystal substrates. $Bi(phenyl)_3$, $Fe(tmhd)_3$ and $Dy(hfa)_3$diglyme (phenyl= $-C_6H_5$; H-tmhd=2,2,6,6-tetramethyl-3,5-heptandione; H-hfa= 1,1,1,5,5,5-hexafluoro-2,4-pentanedione; diglyme= bis(2-methoxyethyl) ether) are used as precursors, mixed in a tri-component source. The epitaxial growth of BDFO on STO:Nb is confirmed through X-ray diffraction (XRD), while field emission scanning electron microscopy (FE-SEM) allowed to assess the flat, homogeneous surfaces of deposited films. The effect of Dy-doping, whose amount has been evaluated by means of X-ray photoelectron spectroscopy (XPS) and energy dispersive X-ray analysis (EDX), on ferroelectric, dielectric and pyroelectric properties of BDFO thin films has been investigated. Permittivity and loss tangent have been determined using impedance–capacitance–resistance (LCR) measurements. The correlation between Dy-doping and pyroelectric response of BDFO thin films has been

established by applying an oscillating temperature ramp on the samples. A clear-cut trend has been observed with the best dielectric and pyroelectric properties found at an intermediate Dy doping level.

2. Results and discussion

2.1. Growth and characterization of BFO and BDFO films

A straightforward MOCVD route, using a multi-component precursor mixture, has been applied for the fabrication of pure and doped $BiFeO_3$ films, using the $Bi(phenyl)_3$ and $Fe(tmhd)_3$, as Bi and Fe sources, and the $Dy(hfa)_3$•diglyme to dope $BiFeO_3$ films at the A-site with Dy^{3+}. Three different Dy doping amounts in the precursor mixture have been evaluated by using Dy/(Dy+Bi) molar ratios of 8%, 11% and 15%, giving rise to films with the following compositions (vide infra): $Bi_{0.94}Dy_{0.06}FeO_3$ (from now on BDFO- 6%), $Bi_{0.92}Dy_{0.08}FeO_3$ (BDFO-8%) and $Bi_{0.89}Dy_{0.11}FeO_3$ (BDFO-11%).

2.1.1. Structural characterization.

BDFO structural characteristics have been investigated by XRD, the planes and their reflections are reported considering a pseudocubic structure. In fact, the parent BFO has a rhombohedral structure with a_{rh} = 3.965 Å and α_{rh} = 89.41° but, given the angle of almost 90°, it is usually referred as pseudocubic. Thus, a lattice mismatch of 1.53% at room temperature is expected for the epitaxial $(001)_{pc}$ BFO films on the $SrTiO_3$ substrate having a perovskite cubic structure with an a-axis parameter a_S = 3.905 Å. The θ-2θ XRD patterns of BFO and BDFO are reported in **Figure 1a**. For all samples, pure and Dy-doped BFO, the diffraction patterns show exclusively reflections associated with BFO-like phase and STO:Nb 001 and 002 reflections, thus indicating that highly oriented films are grown without forming any parasitic phases. A closer look to the second order reflections, Figure 1b, reveals structural changes caused by the dopants. Firstly, the increase of the Dy content causes a broadening of the BDFO 002 reflection.

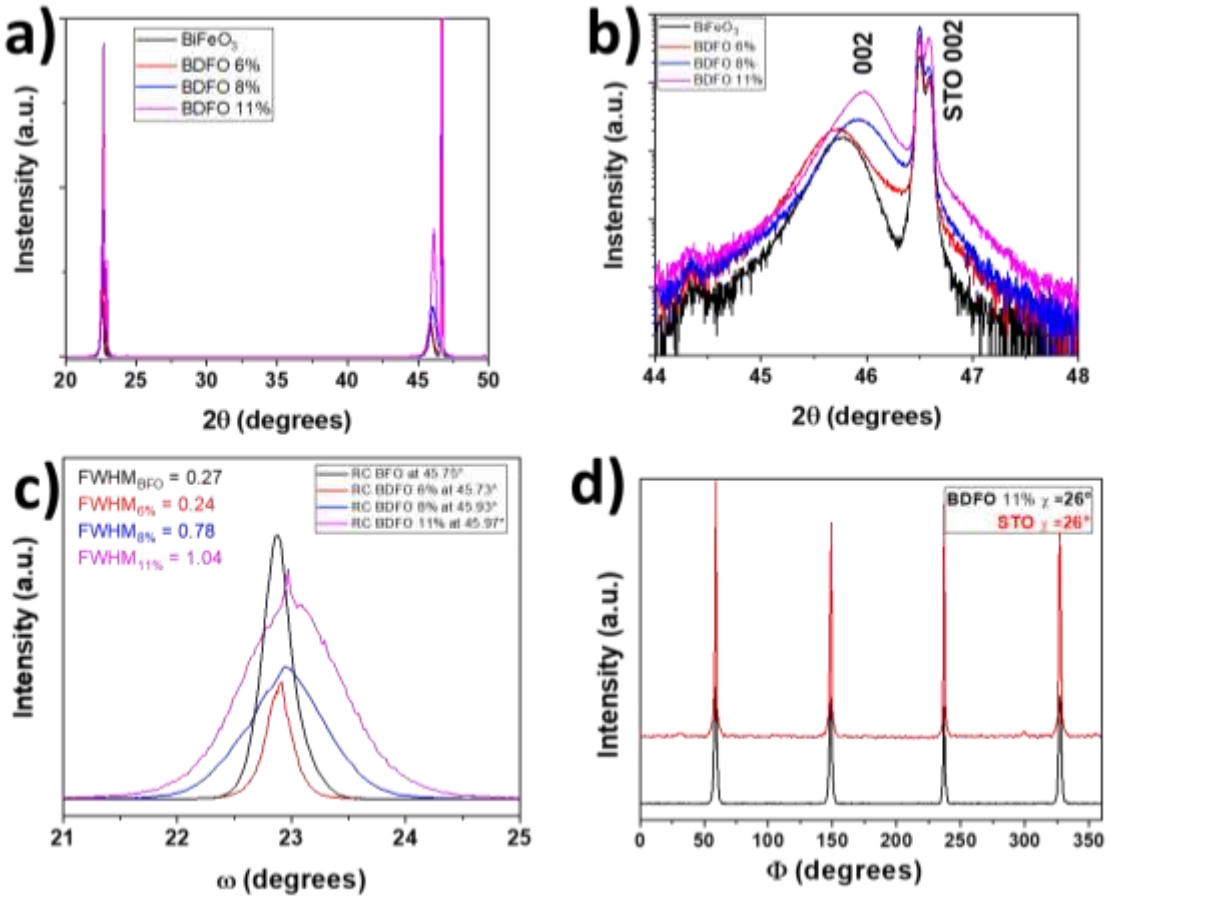

Figure 1 XRD patterns of the doped and undoped BFO films: a) θ-2θ patterns and b) enlarged 2θ region in the 44°-48°; c) rocking curves of the BFO and BDFO films around their 002 reflections; d) φ scan of 210 reflections of the BDFO 11% film and the STO:Nb substrate.

In addition, a shift of the 002 reflections toward higher angles and, consequently, the decrease of the out-of-plane lattice parameter are observed, as the average A-site ionic radius is reduced when the smaller Dy^{3+} ($r_{12\text{-}coord}$ = 1.24 Å) replaces Bi^{3+} ($r_{12\text{-}coord}$ = 1.36 Å).[48,49] The film out-of-plane alignment has been confirmed by recording the rocking curves of the 002 reflections of the four studied films. The second order reflections are at the following positions: 45.75°, 45.73°, 45.93°, and 45.97° for the BFO, BDFO-6%, BDFO-8% and BDFO-11%, respectively. The rocking curves and the full width half maximum (FWHM) values of each system have been reported in Figure 1c. Pure BFO and BDFO-6% films show a similar mosaicity, with a FWHM of 0.27° and 0.24°, respectively. At higher doping, the shift of the 002 reflection and its broadening, visible in the θ-2θ patterns, are reflected on the rocking

curves FWHM values of 0.78° and 1.04° for the BDFO-8% and BDFO-11%, respectively. It is worth to note that even if the increasing doping indicates a higher misalignment of film grains, all the films are of high quality, in terms of pure phase and high out-of-plane orientation.

Considering the remarkable out-of-plane alignment, in-plane alignment has been investigated by recording Φ-scans of the BDFO films. A similar study was already performed on BFO deposited on STO (001)[40] demonstrating its epitaxial growth on STO single crystal. Following a similar approach, Φ-scan patterns of the highest doping content film, the BDFO-11% and the STO:Nb substrate have been recorded at χ=26° to observe both BDFO (2θ = 51.52°) and STO:Nb 210 (2θ = 52.33°) reflections (Figure 1d). The presence of four peaks every 90° of Φ indicates that the film is in-plane aligned. The correspondence of the (210) BDFO poles with the STO:Nb (210) poles demonstrates that BDFO films are epitaxially grown cube-on-cube on STO:Nb single crystal substrate.

Finally, to have more insights on the film structure on changing the Dy doping, Bragg-Brentano patterns have been recorded at χ=26° in the range 2θ= 50° to 54° for the 012 reflection of the film and the substrate (**Figure 2**). Pure BFO peak splitting in the 012 and 0-12 reflections assesses the rhombohedral nature of the film. For Dy-doped systems a shift toward higher angles is observed. The extremely broad nature of the diffraction peak suggests the presence of a splitting similar to the one observed for pure BFO. Literature studies report a phase transition from rhombohedral to orthorhombic structure in the case of BFO Dy-doping, with a morphotropic phase boundary around a Dy content of 8%.[50] In the case of BDFO ceramics, a Dy-doping of at least 15% is necessary to determine a transition from the rhombohedral to the orthorhombic phase.[51-53] Thus, the present XRD study confirms a slight structural modification in the films as the Dy doping amount increases. The analyzed films present a rhombohedral structure and the low Dy concentration in the films (11% is the

highest concentration used in the present study) does not induce the transformation to an orthorhombic structure.

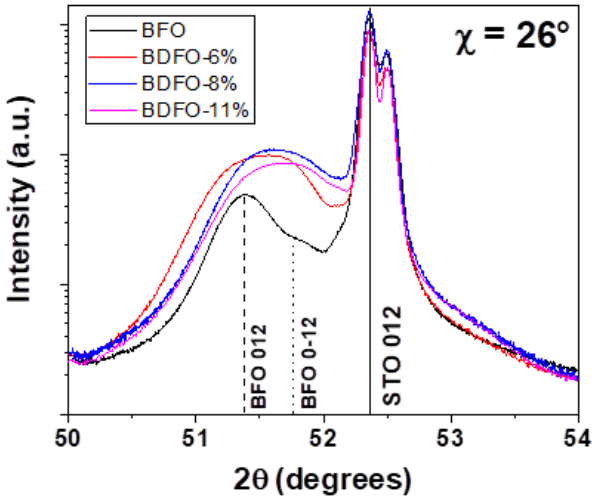

Fig. 2 XRD patterns of the BFO and BDFO thin films acquired in Bragg-Brentano mode (θ-2θ) in the range 50-54° at χ=26°.

2.1.2 Compositional analysis.

This work major aim is to define a relation between the dopant concentration and multifunctional properties. XPS and EDX analyses have been used to assess the presence of Dy in the film and to determine the solid solution average composition. XPS survey scan after 10 min of Ar^+ sputtering is reported in **Figure S1.** The Dy doping is assessed by the presence of the $3d_{5/2}$ peak at 1297.8 eV. Due to the low kinetic energy of the $3d_{5/2}$ derived photoelectrons (188.8 eV) and, in turn, to their low mean free path,[54] Dy detection is strongly affected by the presence of surface overlayers and, therefore, a preliminary 10 min sputtering is needed to clearly detect the Dy $3d_{5/2}$ band. Note that the Dy 4d peak at about 153 eV cannot be detected because of its overlapping with the much more intense Bi 4f signals. Thus, quantitative XPS analysis of Dy is hampered due to the combination of the low mean free path of Dy $3d_{5/2}$ photoelectrons and to the effects of the sputtering process,[54,55] which can induce changes on the surface composition. EDX spectra also confirm the presence of Dy

dopant in the thin film, Figure S2. Two Dy peaks can be observed: M line at 1.29 keV and L_α line at 6.49 keV. The proximity between Dy L_α and Fe K_α (6.39 keV) lines makes precise Dy quantification challenging, but an accurate approach to EDX Dy and Fe quantification makes possible to estimate film composition. Since the EDX software does not allow the use of the Dy M lines for Dy quantification, Dy L_α and Fe K_α lines have to be used for elements quantification. To overcome this problem, an undoped BFO film has been used as a reference to get a conversion coefficient between the Fe K_α and the Fe L line intensity. Then, for Dy-doped films, the study of the ratio between the Fe K_α line and the Fe L line, compared to the reference value obtained for pure BFO sample, allowed us to separate the contribution of the Dy L peak in the quantification of Fe in the films. Table 1 reports the nominal precursor mixture composition, deposited films stoichiometry and overall (Bi+Dy) / Fe ratio in the films. This approach enables to estimate the increase of doping element in the film: interesting is the linear trend between the mixture nominal element composition and the final film composition, which allows, in a flexible and simple way, to predict and finely tune film properties.

Table 1 Relationship between precursor nominal composition and film stoichiometry based on EDX evaluation.

Precursor composition	Film stoichiometry	
	Dy / (Dy + Bi)	(Bi + Dy) / Fe
$BiFeO_3$	0%	0.95
$Bi_{(1-x)}Dy_xFeO_3$ (x = 0.08)	6%	0.96
$Bi_{(1-x)}Dy_xFeO_3$ (x = 0.11)	8%	0.94
$Bi_{(1-x)}Dy_xFeO_3$ (x = 0.15)	11%	0.95

2.1.3. Morphological characterization.

BFO and BDFO film samples, deposited on STO:Nb (5 mm x 10 mm), present mirror-like surface quality. FE-SEM micrographs of the studied films, obtained through detection of secondary electrons, are reported in **Figure 3**. The morphology of pure BFO film is very uniform (Figure 3a) and presents well-coalesced, large, squared grains of about 500 nm in

average. Dy-doped BFO films, with increasing Dy doping from 6% to 11%, are reported in Figure 3b, c, d, respectively, and show an even smoother morphology with a flat surface formed by fully coalesced regular grains; thus, the increase of doping content seems to generally improve film morphology.

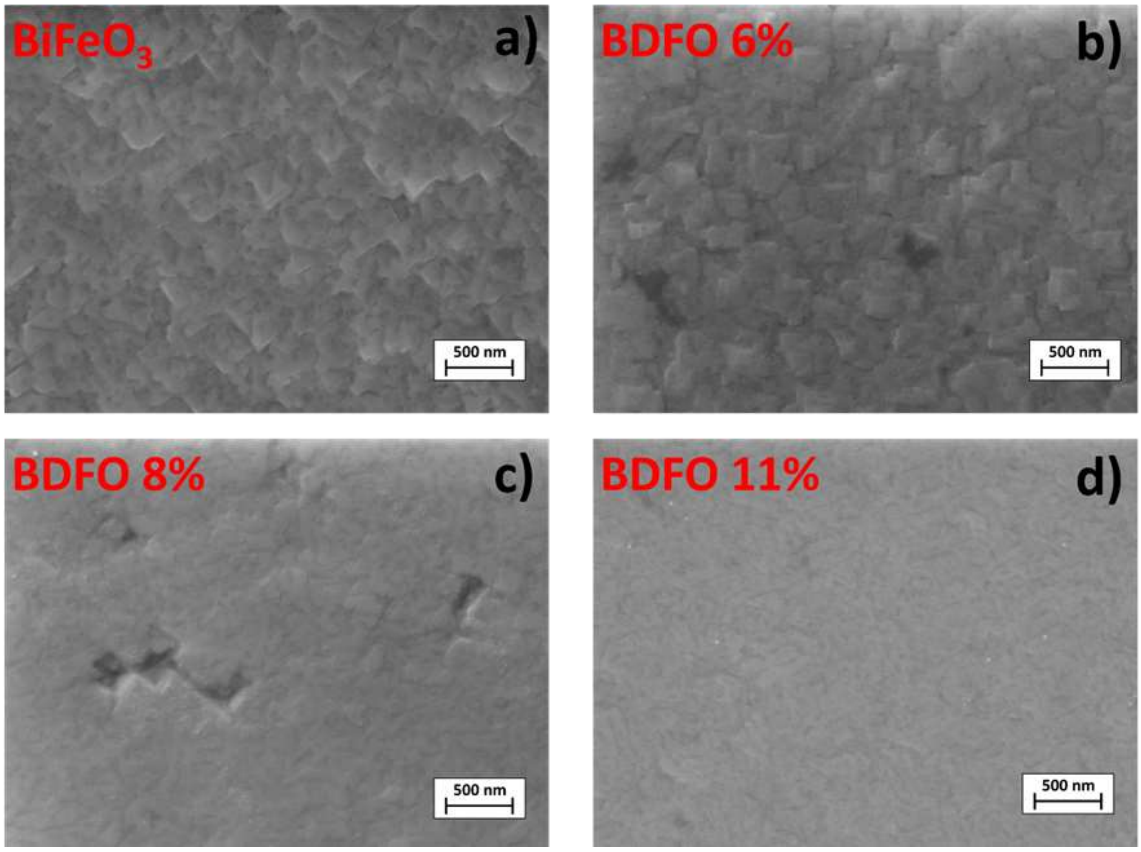

Fig. 3 Secondary electron FE-SEM plan view images of a) $BiFeO_3$, b) BDFO 6%, c) BDFO 8%, and d) BDFO 11%.

Finally, sample thickness has been checked through FE-SEM cross-sections. The thicknesses of both BFO and BDFO samples are in the range of 450-500 nm for a 1-hour MOCVD process, indicating a similar growth rate of 8 nm min^{-1} (**Figure 4**).[35]

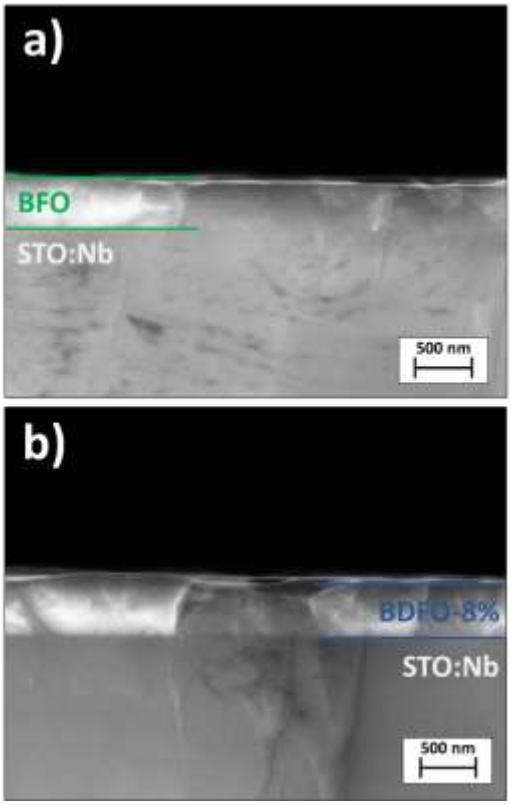

Figure 4. Secondary electron FE-SEM cross section of a) $BiFeO_3$ and b) BDFO-8%.

2.2. Functional properties of BFO and BDFO

2.2.1. P-E unipolar loops.

The polarization-electric field (P-E) negative unipolar loops have been measured between -200 and 0 kV/cm at 5 kHz to limit leakage current impact on the measurements (the sample had a more important leakage under positive polarity).[56] **Figure 5** reports P-E unipolar loops of 500 nm thick BFO, BDFO-6%, BDFO-8% and BDFO-11% thin films at room temperature. Unipolar loops do not allow ferroelectric switching, thus the film polarizations cannot be measured and compared. All thin film ferroelectric half loops show a rounded tip and an increasing charge with decreasing electric field amplitude, which is common for $BiFeO_3$ systems.[52] This difference with the classical shape of ferroelectric hysteresis loops indicates the presence of leakage currents in the samples. The up-bending of the curve upon returning to zero electric field, however, is due to a ferroelectric response. It is also clear that the films do not switch, which is the case when they had a heavy imprint favoring one direction. As it

becomes even more clear with the pyroelectric characterization, the films are self-poled in direction from the substrate to the top electrode, thus parallel to the negative electric field as used for the half-loop measurements.

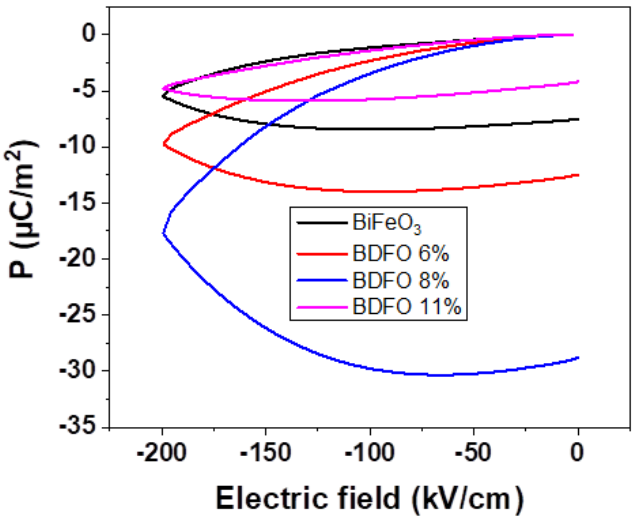

Figure 5. P-E negative unipolar loops of doped and undoped BFO films, measured between -200 and 0 kV/cm at 5 kHz.

As the thin film Dy-doping increases from 6% to 8%, the impact on ferroelectric behavior is more and more visible. For a Dy doping amount superior to 8%, a significant reduction of the BDFO properties has been observed. A similar behavior has been previously reported and attributed to phase transition from a ferroelectric to a paraelectric phase due to the rare-earth doping amount.[1,11,34] Thus, larger ferroelectric contributions are visible for the Dy-doped BFO films, compared to the undoped BFO one, which indicate the strong influence of Dy-doping on material properties.

2.2.2. Permittivity.

Sample relative permittivity (ε_r) and dielectric loss [tan(δ)] at three different frequencies (100 Hz, 1 kHz and 10 kHz) are reported in **Figure 6a**. Sample permittivity values have been calculated from the capacitance measured in parallel plate configuration: (Au/Cr)/BDFO/STO:Nb. Compared to previous studies, pure $BiFeO_3$ films possess a similar relative permittivity value of $\varepsilon_{r\,BFO}$= 130 at 1 kHz, in the literature reported values oscillate

around ε_r = 100, depending on the synthetic method and the measurement frequency.[26,57] The major aspect of this test is to highlight the impact of Dy-doping on the film permittivity. The first two levels of doping (6% and 8%) provoke an important and significant increase of the film permittivity, the highest value of $\varepsilon_{r\ BDFO}$=250 at 1 kHz is obtained for a Dy doping content of 8%.

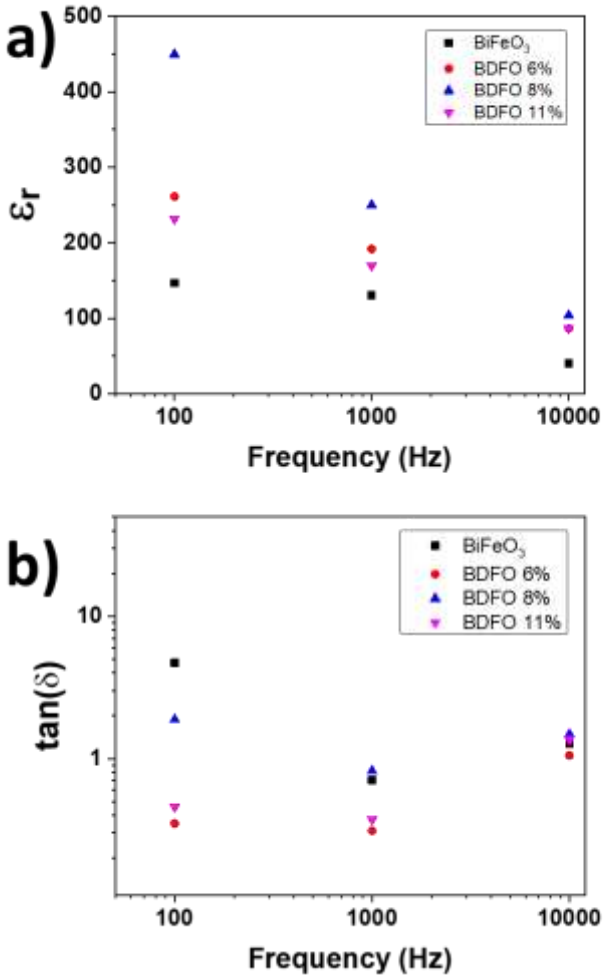

Fig. 6 a) Relative permittivity (ε_r) and b) dielectric loss [tan(δ)] of doped and undoped BFO films, measured at 100 Hz, 1 kHz, 10 kHz.

Above this concentration, similarly to the trend observed during the polarization study of BDFO films, a deterioration of the film permittivity has been detected with a ε_r decrease from 250 to 170 between BDFO-8% and BDFO 11%. Dy-doping also affects dielectric losses of the films at 100 Hz (Fig. 6b). At this frequency, the tan(δ) of BFO is 4.7, while for the BDFO

samples lower losses are observed, of about 0.4 for the 6% and 11% samples and 1.9 for the 8% one.

Pyroelectric properties. The oscillating temperature method was applied for the pyroelectric measurements. While the average temperature was achieved using heating elements, the temperature oscillation was realized with Peltier cooling elements in the substrate chuck. A critical parameter is the homogeneous temperature distribution within the sample. Thus, before starting any measurement, to ensure a homogeneous temperature of the whole sample, temperature equilibrium between the Peltier and the samples had to be achieved.[58] All the four systems, pure and Dy-doped BFO films, have been carefully put into thermal equilibrium and pre-cycled to avoid thermally stimulated currents before their pyroelectric properties were investigated. Samples have been tested "as-deposited", no poling has been performed. Pyroelectric responses of BFO, BDFO 6%, BDFO 8% and BDFO 11% samples are reported in **Figure 7a**, b, c and d, respectively. The setup used for the pyroelectric measurement is shown in Figure S3 and for the sake of clarity a close up view of single pyroelectric measurement cycles for all the samples is reported in Figure S4. Pyroelectric current (in blue) is easily identified because it reverses its sign when the applied temperature ramp (triangular temperature waveforms in black) is reversed. The pyroelectric coefficients were calculated using equation 1:

$$p_i = \frac{i_p}{\frac{dT}{dt} \times A} \qquad \textbf{.Eq1}$$

where p_i , i_p, A and dT/dt are the pyroelectric coefficient, pyroelectric current, area of the electrode and heating rate of the sample, respectively.[58] The technique is based on the variation of the material spontaneous polarization **Δ**P when a change in temperature **Δ**T is applied on it. The polarization change determines a pyroelectric current i_p flowing in an external circuit and depends only on the rate of temperature change (dT/dt).[59] The temperature oscillation method is a well-established method for determining the pyroelectric

coefficient of thin films. Because the causes of thermally stimulated current are various, the dynamic measurement method is quite valuable as it allows to distinguish between reversible and irreversible current responses. Thus, this dynamic method, being the pyroelectric current reversible, allows evaluation of only the pyroelectric current.

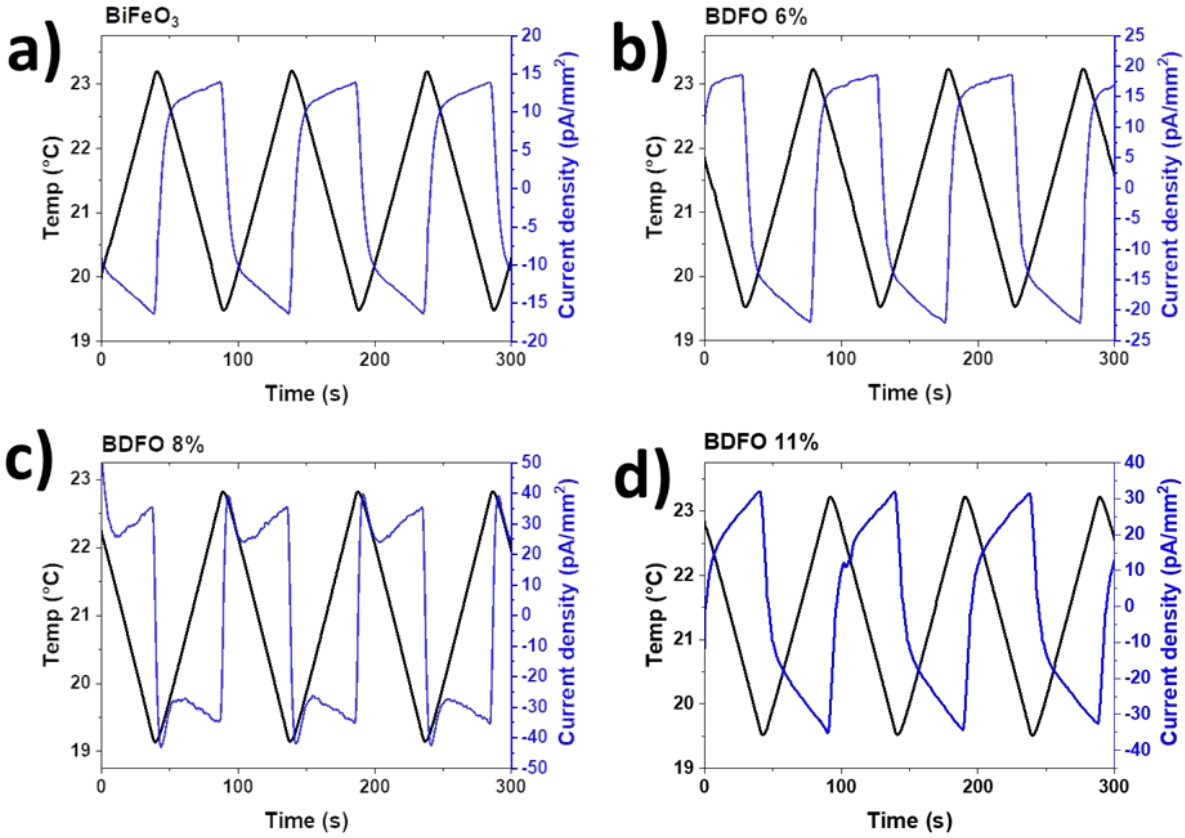

Figure 7. Pyroelectric responses of a) $BiFeO_3$, b) BDFO 6%, c) BDFO 8%, d) BDFO 11% to a triangular temperature waveform ΔT=4 °C at RT.

Moreover, the possibility of choosing the reference temperature is useful to monitor and compare different samples under similar working conditions, here around RT. In the case of distortions in the pyroelectric current curves, this gives information about deposited films.[60] Because of the leakage in the samples, pyroelectric current does not always reach saturation and the cycle curves (Figure 7) are different than the ideal ones (Figure 8). The different shape may be explained considering that domains, i.e. regions of the material with oriented dipoles in the same direction, do not adapt immediately to the change of temperature, because of domain wall traps and build-up of film stress (elastic energy). This slow re-arrangement of

domains gives rise to a smooth increase of the pyroelectric current density at the end of the temperature ramp-up. In contrast, when the temperature goes back to its average value, there is an easy back-switching and a reduction of elastic energy. The polarization reacts immediately, giving rise to an abrupt decrease of the current at the beginning of the temperature ramp and then, again, to a smooth decrease due to the slow domain rearrangement, in the case of samples reported in Figure 7a, b, and d.

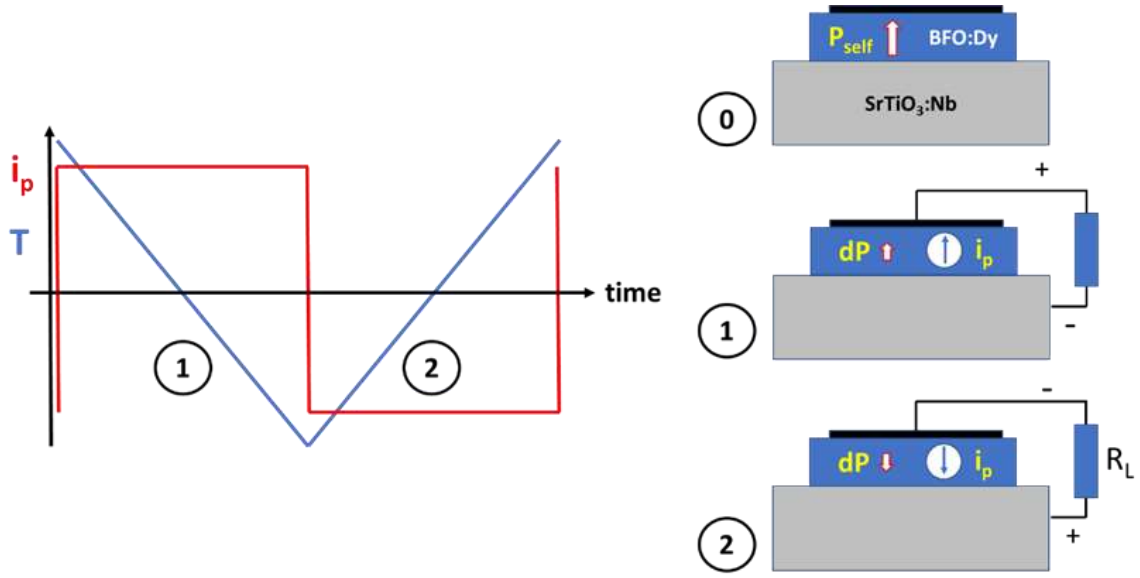

Figure 8 Scheme of the Au/BDFO/STO:Nb behavior under a variation of temperature with 0 the initial state and 1 and 2 the variation of the internal polarization and measured

A similar behaviour is observed for the BDFO 8% sample (Figure 7c), but, in addition, the back-switching seems to be very quick, leading to peaks at the extreme of the temperature ramps due to a kind of overshoot.

Since pyroelectric current does not reach saturation, i_p has not been measured peak-to-peak (Figure 7) and to avoid overestimation of film pyroelectric coefficients, current density slightly lower than i_p peak-to-peak have been selected to calculate the pyroelectric coefficients. This means that the reported values are underestimated with respect to the peak-to-peak derived ones.

Even though samples have a leaky behavior, very good pyroelectric coefficients have been measured, the main hypothesis to explain this phenomenon is that films are self-poled. This is because the generated charges give a much stronger current than the leakage due to a rather small generated voltage governed by the ratio of charge and the rather large dielectric constant. Illustration of the proposed mechanism is presented in **Figure 8,** the evolution of the self-poling direction in the material and the sense of pyroelectric current, as measured when a temperature variation is applied to the films, are detailed.

For each film, the pyroelectric coefficient value has been reported along with the relative permittivity and the figure of merit for pyroelectric energy harvesting application (F_E) in the **Table 2**, which also lists literature data for BFO systems and other materials of interest. F_E is calculated with Equation 2, where ε_0 and ε_r are vacuum permittivity and material relative permittivity, respectively.[62]

Figure of merit values are of great interest to simplify the comparison of materials for a given application. Whatever the electronics for harvesting the pyroelectric energy, the delivered current is governed by the pyroelectric coefficient of the material, and the voltage by the charge on the capacitor (also proportional to p_i) divided by the capacitance, which is proportional to the dielectric constant ($\varepsilon_0\varepsilon_r$), yielding the material's figure of merit for pyroelectric energy harvesting as given in Equation 2.

$$F_E = \frac{p_i^2}{\varepsilon_0 \times \varepsilon_r} \quad \textbf{. Eq2}$$

The pyroelectric response is equal to p_i=dP/dT at a given temperature. An increase of this coefficient is either due to an increase of polarization, or due to a lowering of the ferroelectric transition temperature.[62] As PE loops have shown an increase of ferroelectric features till a nominal Dy doping of 8%, it could indeed be that the polarization increases. Nevertheless, as the composition changes, the second possibility cannot be excluded.

Table 2 Comparison of presently obtained pyroelectric coefficient, permittivity and F_E for the BFO and Dy-doped BFO films with respect to available literature values for BFO, $LiTaO_3$, $LiNbO_3$, PZT and PMN-25PT systems.

System	Synthesis method	Shape	T measurement (°C)	p_i [μC/(m²*K)]	ε_r	F_E [J/(m³K²)]	Ref
$BiFeO_3$	MOCVD	Thin film	RT	188	130 (at 1 kHz)	30.71	This Work
BDFO-6%	MOCVD	Thin film	RT	256	190 (at 1 kHz)	38.96	This Work
BDFO-8%	MOCVD	Thin film	RT	426	250 (at 1 kHz)	81.98	This Work
BDFO-11%	MOCVD	Thin film	RT	288	170 (at 1 kHz)	55.1	This Work
$BiFeO_3$	PLD	Thin film	RT	40	~100 (at 10 kHz)	1.81	Ref. 11
$Bi_{1-x}La_xFeO_3$	PLD	Thin film	RT	85	~240 (at 10 kHz)	3.4	Ref. 11
BFO/PZT (70/30)	sol-gel	Thin film	RT	91	288 (at 1 kHz)	3.25	Ref. 5
BFO/PZT (30/70)	sol-gel	Thin film	RT	5.1	244 (at 1 kHz)	0.02	Ref. 5
$BiFeO_3$	chemical solution	Thin film	RT	15	76 (at 1kHz)	0.33	Ref. 59
$BiFeO_3$	solid-state-reaction	Ceramic	RT	71	~100 (100 kHz)	5.69	Ref. 66
$BiFeO_3$	solid-state-reaction	Ceramic	25	90	-	-	Ref. 65
$Bi_{1-x}Nd_xFeO_3$ (x=0 – 0.15)	solid-state-reaction	Ceramic	RT	30 – 50	100 to 140 (at 1kHz)	1 - 2	Ref. 57
$Bi_{1-x}Sm_xFeO_3$ (x = 0.01– 0.08)	solid-state-reaction	Ceramic	RT	137	120- 140 (100 kHz)	15.1 - 17.66	Ref. 12
$BiFeO_3$	solid-state-reaction	Ceramic	RT	90	103 (1 MHz)	8.88	Ref. 26
$Bi_{1-x}Eu_xFeO_3$ (x=0.05)	solid-state-reaction	Ceramic	RT	133.2	145 (1 MHz)	13,82	Ref. 26
$Bi_{1-x}Gd_xFeO_3$ (x=0.05)	solid-state-reaction	Ceramic	RT	145.5	141 (1 MHz)	16.96	Ref. 26
$Bi_{1-x}Tb_xFeO_3$ (x=0.05)	solid-state-reaction	Ceramic	RT	88	122 (1 MHz)	7.17	Ref. 26
$Bi_{1-x}Dy_xFeO_3$ (x=0.05)	solid-state-reaction	Ceramic	RT	98	128 (1 MHz)	8.47	Ref. 26
Other lead-free systems							
$LiTaO_3$		single crystal		190	47	87	Ref. 7
$LiNbO_3$		single crystal		96	31	34	Ref.66
Lead-based systems							
PZT (Toshiba)		ceramic	RT	350	471	29	Ref.65
PMN- 25 PT		ceramic	RT	602	1648	25	Ref.66
PIMNT	[111]	Single crystal	RT	760	470	139	Ref.67
PZFNTU		Ceramic	RT	400	280	64.4	Ref.68
PMZT	Sol-gel	Thin film	RT	350	253	54.7	Ref.69

While knowledge of pyroelectric properties in BFO ceramic is well established, results regarding thin film characterization are still limited. Previous studies report pyroelectric

values up to 90 μC/(m²K) for undoped BFO ceramics, 91 μC/(m² K) for BFO/PZT thin films, 137 μC/(m² K) for $Bi_{(1-x)}Sm_xFeO_3$ ceramics and 145.5 μC/(m² K) for $Bi_{(1-x)}Gd_xFeO_3$ ceramics.[5,12,26] The undoped BFO thin film deposited in this work displays a pyroelectric coefficient of **188 μC**/(m² K), a value that is higher than any previously reported coefficient for BFO, regardless of the chosen synthetic route.

The explanation for this important increase of the pyroelectric coefficient has to be related to the dense, homogeneous and high-quality nature of the films, made possible by the applied MOCVD protocol used for the sample preparation. In particular, the significant pyroelectric increase with respect to the literature data can be mainly explained considering the epitaxial nature of the grown films, and probably also the self-poling. This observation finds counterpart in the study on textured and epitaxial PZT films. Moalla et al. found that the dynamic pyroelectric coefficient of the epitaxial layer is about one order of magnitude larger than that of the polycrystalline textured layer (−230 vs −30 μC m^{-2} K^{-1}).[70] It is worth mentioning that in ref. 70, pyroelectric devices have been tested dynamically with external stimuli fluctuations (temperature), thus under conditions similar to those applied for evaluating pyroelectric coefficient in this work. Pyroelectric and F_E values of the deposited films are comparable with those reported for the lead-based systems. However, as mentioned above, materials quality plays an important role and in the case of lead indium niobate - lead magnesium niobate - lead titanate (PIMNT) single crystals F_E values as high as 139 have been measured.[67-69]

As expected, Dy-doping has a strong impact on film pyroelectric behavior, which follows a similar trend to that observed in the P-E measurements. For a Dy doping of 8% a maximum value of p_i = **426** μC/(m² K) is found, which is more than twice the value of the pure BFO film. Efficiency for energy harvesting is conveniently compared thanks to the figure of merit F_E which includes the effect of the relevant materials properties, i.e. pyroelectric coefficient and permittivity. Ideally, the improvement of pyroelectric generators would target an

enhanced pyroelectric coefficient and a reduced permittivity. The presently reported undoped BFO films already show similar F_E as PZT and PMN-25PT, the standard materials to benchmark good quality lead-free materials.[65,66] Although a certain increase of the film permittivity is observed till a Dy-doping of 8%, the much stronger increasing pyroelectric response gives rise to a F_E as high as 82 J/(m^{3}K^2) for the BDFO-8%. With such outstanding properties, a performance equivalent to single crystal $LiTaO_3$ is reached.[7] **Figure 9** illustrates the relation between pyroelectric coefficients and F_E values obtained for presently deposited films with some p_i and F_E data from the literature for BFO based systems and other materials of interest providing a perspective of the complexity in comparing these data that depend not only on the measurement approach, but also on the aggregation nature, single crystals, ceramics or films, and in this case on the deposition methodology.

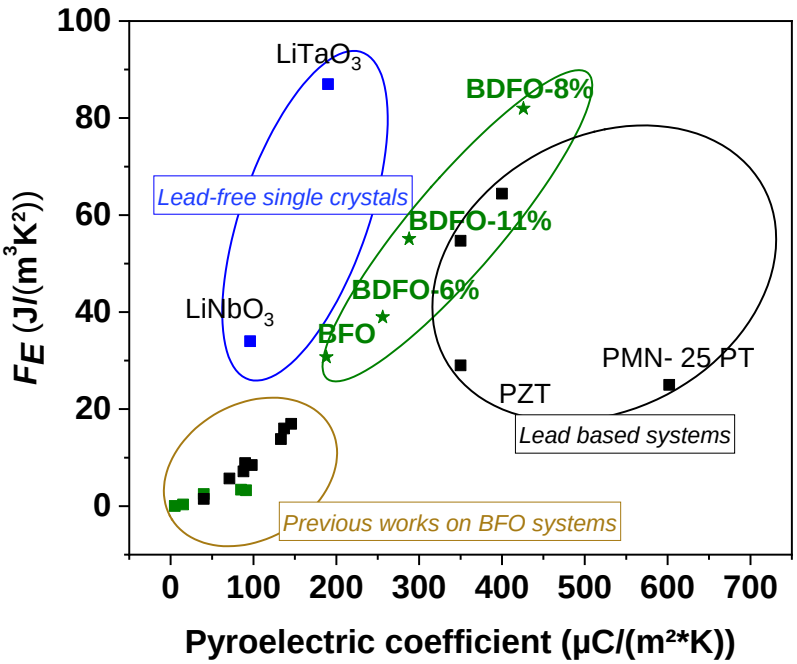

Figure 9. Comparison between pyroelectric coefficients and F_E obtained in this work (green stars grouped in the circle) and previous values of BFO related systems (films (green) and ceramics (black)), lead based systems and lead-free single crystals.

3. Conclusions

The main aim of the present study is to determine if dense films of undoped and Dy-doped $BiFeO_3$, as deposited on STO:Nb (100) through a simple, industrially appealing MOCVD route, may be integrated as lead-free pyroelectric energy harvester. Thus, ferroelectric, dielectric and pyroelectric properties of $Bi_{1-x}Dy_xFeO_3$ (x = 0, 0.06, 0.08 and 0.11) thin films have been investigated. An extraordinary high pyroelectric coefficient of 188 μC/(m² K) has been found for the undoped BFO film, an indication of the possible self-poling and the high quality of the epitaxial films grown by MOCVD. Dy^{3+} substitution has been shown to lead to a large increase of pyroelectric properties with respect to the undoped system. A very high value of the pyroelectric coefficient of 426 μC/(m² K) has been achieved for the 8% Dy^{3+} doping. Above this concentration, pyroelectric properties start to degrade. The presently found pyroelectric coefficients are significantly higher than those reported in the literature and the figure of merit values for energy harvesting are impressively promising. In fact, the obtained F_E value of 82 J/(m^3 K^2) for the BDFO-8% sample, is a striking improvement with respect to the previously highest reported value of F_E = 17 J/(m^3 K^2) for a $Bi_{1-x}Sm_xFeO_3$ ceramic sample. The very appealing and excellent properties reported in this study indicate that the presently described, straightforward and facile MOCVD synthetic route produces high quality epitaxial BFO and BDFO thin films, which can be envisaged as lead-free materials of choice for pyroelectric energy harvesting.

4. Experimental Section

The film depositions were carried out in a customized, horizontal, hot-wall MOCVD reactor. $Bi(phenyl)_3$ and $Fe(tmhd)_3$ precursors were purchased from Strem Chemicals Inc. and used without further purification, while the $Dy(hfa)_3$•diglyme was synthesized in our lab following a similar protocol to that reported in ref. 71. A tri-metallic mixture of the mentioned precursors was placed in an alumina boat and heated at 120 °C. Oxygen and argon were used,

respectively, as reactant and carrier gases, their flows were kept constant for the whole deposition at 150 sccm (standard cubic centimeter per minute) for both species. The depositions were carried out in the temperature range from 750 °C to 800 °C during 60 min. BFO films were deposited on a 5 mm x 10 mm STO:Nb (100) substrate acting at the same time, as bottom electrode for ferroelectric and functional characterization.[40]

XRD patterns were recorded using a Rigaku Smartlab diffractometer, equipped with a rotating anode of Cu K_α radiation operating at 45 kV and 200 mA. Bragg-Brentano patterns were acquired with a resolution step of 0.02°. Film surface morphology was examined by field emission scanning electron microscopy (FE-SEM) using a ZEISS VP 55 microscope. Film atomic composition was analyzed by energy dispersive X-ray analysis (EDX), using an INCA Oxford windowless detector with an electron beam energy of 15 keV and a resolution of 127 eV for the Mn K_α. X-ray photoelectron spectra (XPS) were measured at 45° takeoff angle relative to the surface plane with a PHI 5600 Multi Technique System (base pressure of the main chamber 3 x 10^{-10} Torr). The spectra were excited by Al-Kα radiation. The XPS peak intensities were analyzed after a Shirley background removal. Spectra calibration was achieved by fixing the "adventitious" C 1s peak at 285.0 eV.

Before any functional characterization, 150 nm thick Cr/Au top electrodes (3.84 mm^2) were sputtered on the samples through a hard mask. The dielectric properties were investigated at room temperature through capacitance and loss measurements with an impedance–capacitance–resistance (LCR) meter (Model HP 4284A, Hewlett–Packard, Tokyo, Japan) using 500 mV signal amplitude. Data were taken at three frequencies: 100 Hz, 1 kHz, and 10 kHz. Ferroelectric polarization was investigated with negative half loops at a cycle frequency of 5 kHz. This unipolar operation was chosen to limit the impact of leakage currents.[56] Measurements are the results of 20 average loops under an applied field from -200 to 0 kV/cm. Measurements of the pyroelectric coefficient were carried out using a classic dynamic temperature cycling method. In this approach, the pyroelectric current between the film top

and bottom electrodes was registered upon subjecting the film to a triangular temperature oscillation of ± 2 °C around room temperature (RT = 22 °C).[72] A cycle frequency of 10 mHz was applied. The slow heating rate of 0.08 °C/s, coupled with the small substrate thickness, 0.5 mm, enables a good and homogeneous thermal transfer across the whole sample.

Supporting Information

Supporting Information is available from the Wiley Online Library or from the author.

Acknowledgements

This work is supported by the European Community under the Horizon 2020 Programme in the form of the MSCA-ITN-2016 ENHANCE project, Grant Agreement N.722496. The authors thank the Bio-nanotech Research and Innovation Tower (BRIT) laboratory of the University of Catania (Grant no. PONa3_00136 financed by the Italian Ministry for Education, University and Research, MIUR) for the Rigaku Smartlab diffractometer facility.

Received: ((will be filled in by the editorial staff))
Revised: ((will be filled in by the editorial staff))
Published online: ((will be filled in by the editorial staff))

References

[1] G. Catalan, J.F. Scott, *Adv. Mater.*, **2009**, *21*, 2463–2485.

[2] T. Choi, S. Lee, Y.J. Choi, V. Kiryukhin, S.-W. Cheong, *Science*, **2009**, *324*, 63–66.

[3] A. Queraltó, R. Frohnhoven, S. Mathur. A. Gómez, *Appl. Surf. Sci.*, **2020**, *509*, 144760/1–144760/8.

[4] Y. Ji, T. Gao, L.W. Zhong, *Nano Energy*, **2019**, *64*, 103909/1-103909/9.

[5] J. Seo-Hyeon, L. Sung-Gap, L. Seung-Hwan, *Mater. Res. Bull.*, **2012**, *47*, 409–412.

[6] R. L. Byer, C. B. Roundy, *IEEE Trans. Sonics & Ultrasonics*, **1972**, *19*, 333-338.

[7] H. Hongyin, L. Xi, H. Emil, C. Chao, Z. Hao and L. Li, *J. Mater. Chem. C*, **2020**, *8*, 1494.

[8] Y. Yang, W. Guo, K. C. Pradel, G. Zhu, Y. Zhou, Y. Zhang, Y. Hu, L. Lin, Z. L. Wang, *Nano Lett.*, **2012**, *12*, 2833–2838.

[9] G.T Hwang, V. Annapureddy, J.H. Han, D.J. Joe, C. Baek, D.Y Park, D.H. Kim, J.H. Park, C.K. Jeong, K.-I. Park, C.K. Jeong Kwi-Il Park, J.J Choi, J.D. Kyung, K.J. Ryu, K.J. Let, *Adv. Energy Mater.*, **2016**, ***6***, 1600237/1–1600237/9.

[10] P. Muralt, R.G. Polcawich, S. Trolier-McKinstry, *MRS Bulletin*, **2009**, ***34***, 658–664.

[11] L. Zhang, Y.L. Huang, G. Velarde, A. Ghosh, S. Pandya, D. Garcia, R. Ramesh, L.W. Martin, *APL Mater.*, **2019**, *7*, 111111.

[12] Q. Wang, C.R. Bowen, W. Lei, H. Zhang, B. Xie, S. Qiu, M.Y. Li, S. Jiang, *J. Mater. Chem. A*, **2018**, *6*, 5040-5051.

[13] Y. Zhang, M. Xie, J. Roscow, Y. Bao, K. Zhou, D. Zhang, C.R. Bowen, *J. Mater. Chem. A*, **2017**, *5*, 6569.

[14] G. Clementi, G. Lombardi, S. Margueron, M.A. Suarez, E. Lebrasseur, S. Ballandras, J. Imbaud, F. Lardet-Vieudrin, L. Gauthier-Manuel, B. Dulmet, M. Lallart, A. Bartasyte, *Mech. Syst. Signal Proc.*, **2021**, *149*, 107171.

[15] A. Almirall, S. Oliveri, W. Daniau, S. Margueron, T. Baron, P. Boulet, S. Ballandras, S. Chamaly, A. Bartasyte, *Appl. Phys. Lett.*, **2019**, ***114***, 162905/1–162905/5.

[16] G. Clementi, S. Margueron, M.A. Suarez, T. Baron, B. Dulmet, A. Bartasyte, *J. Phys.: Conf. Ser.*, **2019**, ***1407***, 012039.

[17] A. Tkach, A. Santos, S. Zlotnik, R. Serrazina, O. Okhay, I. Bdikin, M.E. Costa, P.M. Vilarinho, *Nanomaterials*, **2019**, *9*, 1600.

[18] G. Vats, A. Chauhan, R. Vaish, *Int. J. Appl. Ceram. Technol.*, **2015**, *12*, E49–E54.

[19] A. Kumar, A. Sharma, R, Kumar, R. Vaish, V.S. Chauhan, *J. Asian Ceram. Soc.*, **2014**, *2*, 139–143.

[20] J.V Vidal, A.V. Turutin, I.V Kubasov, A.M. Kislyuk, M.D. Malinkovich, Y.N. Parkhomenko, S.P. Kobeleva, O.V. Pakhomov, N.A. Sobolev, A.L. Kholkin, *IEEE T Ultrason. Ferr.*, **2019**, *66*, 1480–1487.

[21] T. Yoshimura, S. Murakami, K. Wakazono, K. Kariya, N. Fujimura, *Appl. Phys. Express*, **2013**, *6*, 051501.

[22] M. Aramaki, T. Yoshimura, S. Murakami, K. Satoh, N. Fujimura, *Sens. Actuat. A-Phys.*, **2019**, *291*, 167–173.

[23] L. Haitao, C.S. Lin Koh, Y.H. Lee, Y. Zhang, G.C. Phan-Quang, C. Zhu, Z. Liu, Z. Chen, H.Y. Fan Sim, C.L. Lay, Q. An, X.Y. Ling, *Nano Energy*, **2020**, *73*, 104723.

[24] J. Ma, J. Ren, Y. Jia, Z. Wu, L. Chen, N.O. Haugen, H. Huang, Y. Lieu, *Nano Energy*, **2019**, *62*, 376–383.

[25] Paul Muralt, *Rep. Prog. Phys.*, **2001**, ***64***, 1339.

[26] Y. Yao, W. Liu, Y. Chan, C. Leung, C. Mak, B. Ploss, *Int. J. Appl. Ceram. Technol.*, **2011**, *8*, 1246–1253.

[27] J. T. Heron, D. G. Schlom, R. Ramesh, *Appl. Phy. Rev.*, **2014**, *1*, 021303.

[28] C. H. Chiu, W. I Liang, C. W. Huang, J.Y. Chen, Y.Y. Liub, J.Y. Li, C.L. Hsin, Y.H. Chu, W.W.Wu, *Nano Energy*, **2015**, *17*, 72-81.

[29] J. Wang, J. B. Neaton, H. Zheng, V. Nagarajan, S. B. Ogale, B. Liu, D. Viehland, V. Vaithyanathan, D. G. Schlom, U. V. Waghmare, N. A. Spaldin, K. M. Rabe, M. Wuttig, R. Ramesh, *Science*, **2003**, *299*, 1719-1722.

[30] H. Zhu, X. Sun, L. Kang, M. Hong, M. Liu, Z. Yu, J. Ouyang, *Scripta Mater.*, **2016**, *115*, 62–65.

[31] C.S. Tu, P.Y. Chen, C.S. Chen, C.Y. Lin, V.H. Schmidt, *J. Europ. Cer. Soc.*, **2018**, *38*, 1389-1398.

[32] S. Hohenberger, J.K. Jochum, M. J. Van Bael, K. Temst, C. Patzig, T. Höche, M. Grundmann, M. Lorenz, *Materials*, **2020**, *13*, 197.

[33] C. Jin, W. Geng, L. Wang, W. Han, D. Zheng, S. Hu, M. ye, Z. Xu, Y. Ji, J. Zhao, Z. Chen, G. Wang, Y. Tang, Y. Zhu, X. Ma, L. Chen, *Nanoscale*, **2020**, *12*, 9810-9816.

[34] M. R. Catalano, G. Spedalotto, G.G. Condorelli, G. Malandrino, *Adv. Mater. Interfaces*, **2017**, ***4***, 1601025.

[35] A. Radojković, D.L. Golić, J. Ćirković, Z.M. Stanojević, D. Pajić, F. Torić, A. Dapčević, P. Vulić, Z. Branković, G. Branković, *Ceram. Int*, **2018**, *44*, 16739-16744.

[36] T. Zheng, J. Wu, *Adv. Electron. Mater.*, **2020**, *6*, 2000079.

[37] G. Tian, S. Ojha, S. Ning, X. Gao, C.A. Ross, *Adv. Electron. Mater.*, **2019**, *5*, 1900012/1–1900012/8.

[38] H. Pan, Y. Zeng, Y. Shen, Y.H. Lin, J. Ma, L. Li ,C.W. Nan, *J. Mater. Chem. A*, **2017**,*5*, 5920-5926.

[39] G.G. Condorelli, M.R. Catalano, E. Smecca, R. Lo Nigro, G. Malandrino, *Surf. Coat. Technol.*, **2013**, *230*, 168–173.

[40] J. A. S. Moniz, R. Quesada-Cabrera, C.S. Blackman, J. Tang,P. Southern, P. M. Weaver, J. C. Carmalt, *J. Mater. Chem. A*, **2014**, *2*, 2922-2927.

[41] N. Deepak, P. Carolan, L. Keeney, P.F. Zhang, M.E. Pemble, R.W. Whatmore, *Chem. Mater.*, **2015**, *27*, 6508–6515.

[42] Q. Micard, A. L. Pellegrino, R. Lo Nigro, A. Bartasyte, G. G. Condorelli, G. Malandrino, *J. Mater. Chem. C*, **2020**, *8*, 16168-16179.

[43] Q. Micard, G. G. Condorelli, G. Malandrino, *Nanomaterials*, **2020**, *10*, 630.

[44] H. Zhu, Y. Zhao, Y. Wang, *J. Alloys Comp.*, **2019**, *803* 942–949.

[45] P. Hou, B. Liu, Z. Guo, P. Zhou, B. Wang, L. Zhao, *J. Alloys Comp.*, **2019**, *775*, 59–62.

[46] N. Sheoran, A. Kumar, V. Kumar, A. Banerjee, *J. Supercond. Nov. Magn.*, **2020**, *7*, 2017-2029.

[47] C. Xuemei, H. Guangda, Y. Jing, W. Xi, Y. Changhong, W. Weibing, *J. Phys. D Appl. Phys.*, **2008**, *41*, 225402/1–225402/5.

[48] Y. Q. Jia, *J. Solid State Chem.*, 1991, **95**, 184-187.

[49] T. Durga Rao, T. Karthik, S. Asthana, *J. Rare Earths*, **2013**, ***31***, 370-375.

[50] C.H. Yang, D. Kan, I. Takeuchi, V. Nagarajand, J. Seidel, *Phys. Chem. Chem. Phys.*, **2012**, *14*, 15953–15962.

[51] V. A. Khomchenko, D. V. Karpinsky, A. L. Kholkin, N. A. Sobolev, G. N. Kakazei, J. P. Araujo, I. O. Troyanchuk, B.F.O. Costa, J. A. Paixão, *J. Appl. Phys*, **2010**, *108*, 074109.

[52] M. Muneeswaran, N. V. Giridharan, *J. Appl. Phys*, **2014**, *115*, 214109.

[53] Kumar, P. Sharma, D. Varshney, *J. Ceramics*, **2015**, *8*, 869071.

[54] M. P. Seah, in *Practical Surfaces Analysis, vol. 1*, D(Eds. D. Briggs, M.P. Seah) Wyley-VCH, Weinheim, Germany, **1995**, p 201.

[55] N. Q. Lam, *Surf. Interface Anal.*, **1988**, *12*, 65-77.

[56] S. K. Singh, K. Maruyama, H. Ishiwara, *Integrated Ferroelectrics*, **2008**, *97*, 83–89.

[57] G. L. Yuan, S.W. Or, *Appl. Phys. Lett.*, **2006**, *88*, 062905.

[58] S. Jachalke, E. Mehner, H. Stöcker, J. Hanzig, M. Sonntag, T. Weigel, T. Leisegang, D. C. Meyer, *Appl. Phys. Rev.*, **2017**, *4*, 021303.

[59] A. Chynoweth, *J. Appl. Phys.*, **1956**, 27(1), pp.78-84.

[60] M. Daglish, *Integrated Ferroelectrics*, **1998**, *22*, 473–488.

[61] Y.W. Li, J.L. Sun, J. Chen, X.J. Meng, J.H. Chu, *J. Cryst. Growth*, **2005**, *285***,** 595–599.

[62] Y. Yao, T. Tao, B. Liang, C.L. Mak, S.G. Lu, *Ceram. Int.*, **2019**, *45*, 1308-1313.

[63] Y. Yao, B. Ploss, C.L. Mak, K.H. Wong, *Appl. Phys. A*, **2009**, *99*, 211–216.

[64] C. R. Bowen, J. Taylor, E. Le Boulbar, D. Zabek, A. Chauhan, R. Vaish, *Energy Environ. Sci.*, **2014**, *7*, 3836-3856.

[65] H. He, X. Lu, E. Hanc, C. Chen, H. Zhang, L. Lu, *J. Mater. Chem. C*, **2020**, 8, 1494-1516.

[66] J. Kim, S. Yamanaka, A. Nakajima, T. Katou, Y. Kim, T. Fukuda, K. Yoshii, Y. Nishihata, M. Baba, M. Takeda, N. Yamada, T. Nakayama, K. Niihara, H. Tanaka, *Ferroelectrics*, **2017**, *512*, 92-9.

[67] A. Movchikova, A. Günther, N. Neumann, M. Heinze, *Technisches Messen*, **2014**, 81, pp.120-126.

[68] R.W. Whatmore, F.W Ainger, *Proc. SPIE-The International Society for Optical Engineering*, **1983**, 395, 261-6.

[69] R.W. Whatmore, Q. Zhang, Z. Huang, R.A. Dorey, *Mater. Sci. Semicond. Processing*, **2003**, 5, 65–76

[70] R. Moalla, B. Vilquin, G. Saint-Girons, G. Le Rhun, E. Defay, G. Sebald, N. Baboux, R. Bachelet, *Nano Energy*, **2017**, *41*, 43-48.

[71] G. Malandrino, I. L. Fragala, Coord. Chem. Rev., **2006**, *250*, 1605-1620.

[72] M. Davis, D. Damjanovic, N. Setter, *J. Appl. Phys.*, **2004**, *96*, 2811-2815.